

The Dysferlin C2A Domain Binds PI(4,5)P2 and Penetrates Membranes

Ethiene Kwok^{1#}, Shauna C. Otto^{1#}, Patricia Khoo¹, Andrew P. Carpenter³, Sara J. Coddling¹, Patrick N. Reardon², Juan Vanegas¹, Tanushri M. Kumar¹, Chapman J. Kuykendall¹, Ryan A. Mehl¹, Joe Baio³ and Colin P. Johnson^{1*}

1 - Department of Biochemistry and Biophysics, Oregon State University, Corvallis, OR 97331, USA

2 - NMR Facility, Oregon State University, Corvallis, OR 97331, USA

3 - Department of Chemical Engineering, Oregon State University, Corvallis, OR 97331, USA

Correspondence to Colin P. Johnson:*Department of Biochemistry and Biophysics, Oregon State University, Corvallis, OR 97331, USA. colin.johnson@oregonstate.edu (C.P. Johnson)

<https://doi.org/10.1016/j.jmb.2023.168193>

Edited by Ichio Shimada

Abstract

Dysferlin is a large membrane protein found most prominently in striated muscle. Loss of dysferlin activity is associated with reduced exocytosis, abnormal intracellular Ca²⁺ and the muscle diseases limb-girdle muscular dystrophy and Miyoshi myopathy. The cytosolic region of dysferlin consists of seven C2 domains with mutations in the C2A domain at the N-terminus resulting in pathology. Despite the importance of Ca²⁺ and membrane binding activities of the C2A domain for dysferlin function, the mechanism of the domain remains poorly characterized. In this study we find that the C2A domain preferentially binds membranes containing PI(4,5)P2 through an interaction mediated by residues Y23, K32, K33, and R77 on the concave face of the domain. We also found that subsequent to membrane binding, the C2A domain inserts residues on the Ca²⁺ binding loops into the membrane. Analysis of solution NMR measurements indicate that the domain inhabits two distinct structural states, with Ca²⁺ shifting the population between states towards a more rigid structure with greater affinity for PI(4,5)P2. Based on our results, we propose a mechanism where Ca²⁺ converts C2A from a structurally dynamic, low PI(4,5)P2 affinity state to a high affinity state that targets dysferlin to PI(4,5)P2 enriched membranes through interaction with Tyr23, K32, K33, and R77. Binding also involves changes in lipid packing and insertion by the third Ca²⁺ binding loop of the C2 domain into the membrane, which would contribute to dysferlin function in exocytosis and Ca²⁺ regulation.

Published by Elsevier Ltd.

Introduction

Ferlins are a family of large (>200 kDa) transmembrane proteins which contribute to a diverse set of membrane trafficking processes.^{1,2} Among the ferlin family, dysferlin (dysf) is a ~237 kDa protein which localizes to the sarcolemma and t-tubule of striated muscle.^{3,4} Mutations within dysf are associated with pathology,

including limb-girdle muscular dystrophy and Miyoshi myopathy.^{5,6} Dysf knockout models display defective muscle repair and abnormal accumulation of unfused vesicles at the site of sarcolemma membrane injury.⁷ Loss of dysf also results in decreased voltage-triggered Ca²⁺ transients and increased cytoplasmic Ca²⁺ upon injury, which may contribute to pathology.⁴ It is therefore thought that dysf contributes to vesicle docking and fusion during the

repair of damaged plasma membrane, as well as stress-induced Ca^{2+} signaling. A role for dysf in t-tubule biogenesis has also been proposed.⁸ Outside of striated muscle dysf is expressed in arterial endothelial cells where it contributes to lysosome exocytosis and membrane raft clustering in response to Fas Ligand stimulation.⁹

Dysf is predicted to consist of 7 C2 domains and a single pass transmembrane domain (Figure 1(A, B)).^{10,11} Typically C2 domains are composed of up to 130 amino acids and fold into a beta-sandwich, with loops at one end of the domain interacting with membranes and in some cases penetrating the bilayer.¹² Differences in the lipid binding specificity of a C2 domain are thought to underlie the targeting of proteins to specific subcellular membrane compartments within the cell.^{13,14} In addition, the membrane-binding loops for some, but not all C2 domains interact with 2–3 Ca^{2+} ions, conferring Ca^{2+} sensitivity to the membrane binding activity of the domain.¹⁵ For dysf, isothermal titration calorimetry and liposome co-sedimentation studies have identified several Ca^{2+} and phosphatidylserine interacting C2 domains.^{16,17} Unlike other C2

domains within dysf however, the C2A domain at the N-terminus of the protein is distinguished in having been reported to interact with both Ca^{2+} and the phosphoinositide phosphatidylinositol 4,5-bisphosphate (PI(4,5)P2).¹⁷ This domain is separated from the next C2 domain (C2B) by a long intrinsically disordered linker greater than 100 amino acids in length (Figure 1(B)).^{10,11} Within muscle, the C2A domain appears to play an important role for both membrane repair and recovery of Ca^{2+} transients after cell injury. Truncation of the domain results in a reduction of dysf activity, and several mutations within the C2A domain are linked to human disease, highlighting the importance of the domain for dysf function.^{18,19} Peptide-based inhibition studies have also suggested an important role for C2A in lysosome fusion in arterial endothelial cells.⁹ Other ferlin homologues lack a C2A domain (Fer1L6) or possess a C2A domain that does not bind Ca^{2+} (otoferlin) suggesting functional diversity at the N-terminus among the family.^{20,21}

Despite the importance of the C2A domain for dysf activity, the functional properties of the domain remain unclear. Further, while protein

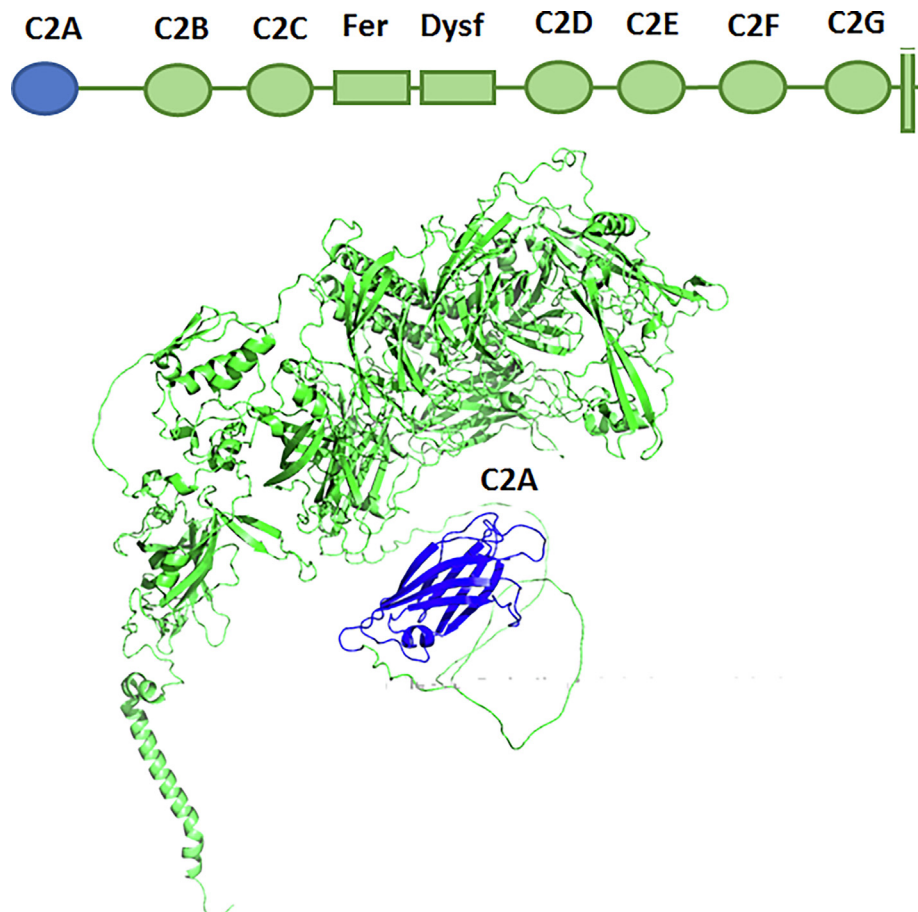


Figure 1. Dysferlin. (Top) Diagram of dysf showing the location of the 7 C2 domains (C2A-C2G), FerA domain, dysf domain, and single pass transmembrane domain (TMD). (Bottom) Dysferlin structure predicted by AlphaFold. The C2A domain is highlighted in blue.

crystallography and NMR studies of C2A have provided a model for Ca²⁺ binding, the structural basis for C2A interaction with PI(4,5)P2 remains unknown.^{15,22} In this study we find that PI(4,5)P2 directs the dysf C2A domain preferentially to target membranes and identify the PI(4,5)P2 interacting residues. Further, we find that Ca²⁺ promotes insertion of the third Ca²⁺ binding loop into membranes. Based on or results we propose a model whereby Ca²⁺ promotes targeting of C2A to PI(4,5)P2 lipids, with insertion of the domain into the bilayer anchoring dysf to the membrane.

Results

Dysf C2A preferentially targets membranes containing PI(4,5)P2

Previous studies have identified dysf C2A as a domain capable of interacting with Ca²⁺, PI(4,5)P2 and phosphatidylserine (PS).^{16,17} Although phosphatidylserine lipids reside in multiple membrane compartments, PI(4,5)P2 is preferentially enriched at the cell membrane and can recruit proteins.²³ For example, the PI(4,5)P2 binding activity of the C2 domain of protein kinase C (PKC) steers the protein to the plasma membrane.¹³ We tested whether C2A is preferentially recruited to membranes containing PI(4,5)P2 using a competition assay.²⁴ In this experiment, we first mixed recombinant C2A with liposomes composed of phosphatidylcholine (PC):phosphatidylserine (PS): and PI(4,5)P2 and the solvatochromic fluorescent membrane probe laurdan (69:25:5:1) (Figure 2(A,B)). Consistent with previous results with ferlin C2 domains, addition of C2A to liposome samples resulted in a blueshift in the laurdan emission which we quantitated by calculating the general polarization (GP) value (0.034, SD = ±0.001 before addition of C2A, 0.145 SD = ±0.006 after C2A addition).^{17,18,25} We next mixed C2A with samples containing both the PC:PS:PI(4,5)P2:laurdan liposomes as well as nonfluorescent PC:PS (75:25) liposomes lacking laurdan (Figure 2(B)). If C2A distributes evenly between both sets of liposomes a smaller shift in the laurdan fluorescence would be expected (Figure 2(B)). However we found that the shift in laurdan spectra for the mixed liposome sample was similar to that of samples containing only PI(4,5)P2 liposomes (Figure 2(C), 0.145, SD = ±0.006 for PI(4,5)P2 containing liposomes only vs. 0.130 SD = ±0.01 for mixed liposome samples). This suggests that the C2A domain preferentially bound to PI(4,5)P2 liposomes and did not distribute between both sets of liposomes. By contrast, measurements conducted with dysf C2B resulted in a lesser GP value for mixed liposome samples relative to samples containing only PI(4,5)P2 liposomes (Figure 2(C), 0.116 SD = ±0.006 for PI(4,5)P2 containing liposomes only vs. 0.060 SD = ±0.01 for mixed liposome samples), suggesting that this domain distributed

between both sets of membranes. Thus, dysf C2A, but not C2B displays sensitivity to the addition of PI(4,5)P2 to PS:PC liposome membranes.

The dysf C2A-membrane binding geometry differs between PI(4,5)P2 and phosphatidylserine membranes

Having found that dysf C2A preferentially binds PI(4,5)P2, we next sought to characterize the C2A-membrane interface using vibrational sum-frequency (VSF) spectroscopy. VSF is a surface specific spectroscopic technique where features related to a protein's amide I modes are sensitive to the structural arrangement of the protein's secondary structure at an interface.²⁶⁻²⁹ We tested C2A-membrane interaction with membrane compositions that allow for comparison to previous reports, with lipid layers composed of different lipid compositions and charge: 3:1 PC:PS, 95:5 PC:PI(4,5)P2, and 70:25:5 PC:PS:PI(4,5)P2 (Figure 3).^{30,31} When measured, we found that the amide I modes between 1630 and 1700 cm⁻¹ varied within spectra taken of C2A at surfaces containing PI(4,5)P2 and those lacking PI(4,5)P2, suggesting that C2A alters its binding geometry at membrane surfaces with PI(4,5)P2 (Figure 3, blue and purple spectra) compared to membranes lacking PI(4,5)P2 (Figure 3, red spectrum). When C2A was bound to the PC:PI(4,5)P2 surface, we observed an increase in VSF signal above 1660 cm⁻¹ relative to the amide I spectrum for C2A at the PC:PS surface. The signal in this spectral region is associated with the B₁ vibration of anti-parallel β-strands and the observed increase suggests C2A has repositioned itself in response to PI(4,5)P2 relative the PC:PS surface.²⁶⁻²⁸ Our previous VSF studies have correlated such a change in intensity to a shift in the C2A tilt angle of nearly 30° with respect to surface normal.³¹ These spectra indicate the C2A domain responds specifically to the presence of PI(4,5)P2 by tilting into an alignment more parallel to the membrane surface. This binding orientation persists even when PS is present alongside PI(4,5)P2, evidenced by the near perfect match between spectra of C2A bound to the PC:PS:PI(4,5)P2 and PC:PI(4,5)P2 surfaces (purple and blue spectra in Figure 3, respectively). Consistent with the laurdan fluorescent experiments, these VSF experiments support a specific interaction between C2A and PI(4,5)P2 at membrane surfaces. To ensure that the observed interaction between C2A and the PI(4,5)P2 lipid membrane is Ca²⁺ sensitive, we repeated our measurements in the presence of either 5 mM Ca²⁺, 50 μM Ca²⁺, or excess EDTA (Figure S1). We found that Ca²⁺ enhanced C2A interaction with a 95:5 PC:PI(4,5)P2 lipid surface, with 5 mM Ca²⁺ providing a more intense amide I vibrational spectra compared to samples containing 50 μM Ca²⁺. Samples with excess EDTA displayed the least signal.

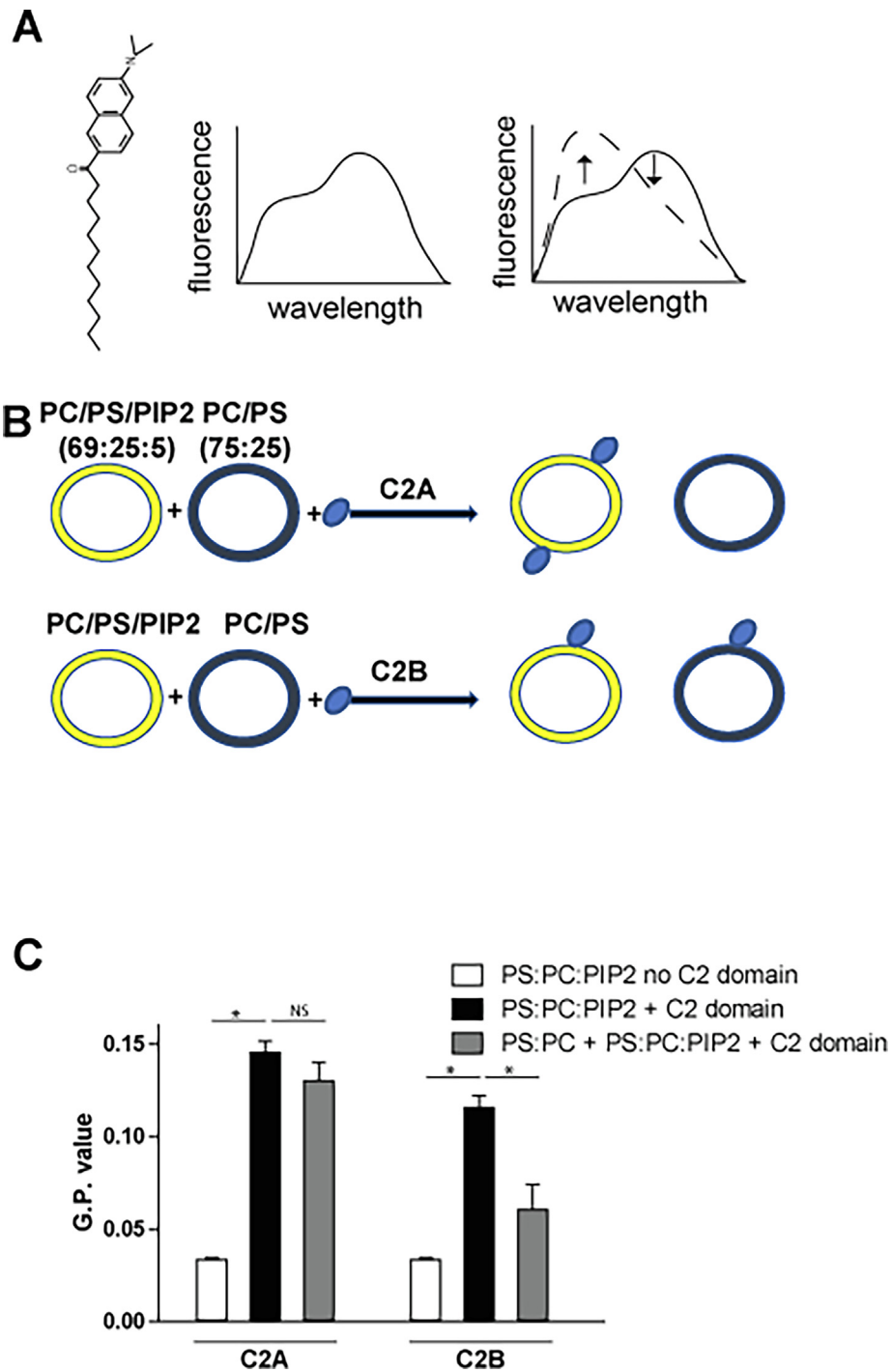


Figure 2. PI(4,5)P2 recruits dysf C2A. (A) Structure of laurdan probe (left) and diagram of changes in laurdan emission spectra upon protein interaction with laurdan-containing liposomes. Arrows denote the changes in wavelength emission associated with C2 domain binding. (B) Diagram illustrating recruitment of C2A to PC:PS:PI(4,5)P2:laurdan (69:25:5:1) containing liposomes preferentially over PC:PS (75:25) liposomes. C2B distributes more evenly between the two sets of liposomes. (C) Mean change in GP values for listed liposome sample. ($N = 3$; error = \pm standard deviation; $*P < 0.01$).

Membrane binding by C2A alters the distance between PI(4,5)P2 molecules

We next tested for the effect of C2A on PI(4,5)P2 containing liposomes by monitoring the

fluorescence of PI(4,5)P2-TopFluor. PI(4,5)P2-TopFluor is a fluorescent analogue of PI(4,5)P2 which self-quenches when brought into close proximity, allowing for changes in distance

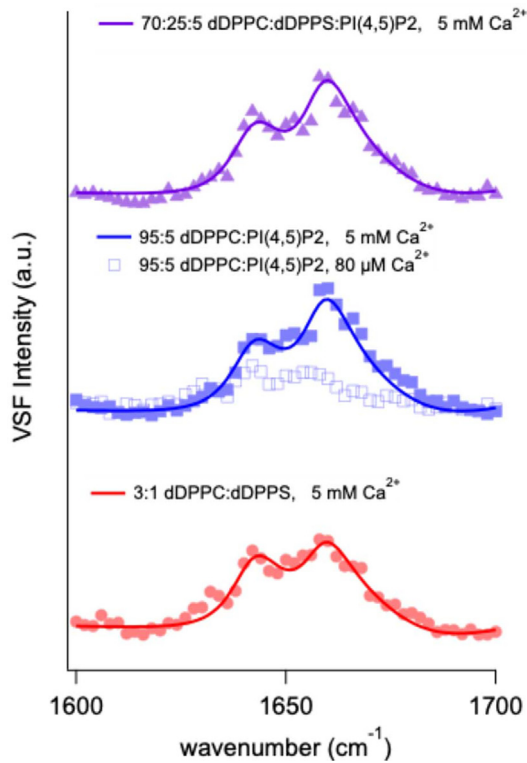


Figure 3. PI(4,5)P2 interaction influences the C2A-membrane binding geometry. VSF spectra of C2A bound to the 3:1 DPPC:DPPS (red circles), 95:5 DPPC:PI(4,5)P2 (blue squares), and 70:25:5 DPPC:DPPS:PI(4,5)P2 (purple triangles) lipid monolayers. Solid lines are spectral fits to the data.

between lipids to be measured in response to C2A interaction with liposomes.³² As shown in Figure 4 (A), fluorescence quenching was observed for liposomes composed of PC:PS:PI(4,5)P2:PI(4,5)P2-TopFluor (70:25:4.5:0.5) liposomes mixed with C2A in the presence of 250 μ M Ca²⁺. We quantitated fluorescence quenching for C2A as well as C2B and found the extent of fluorescence quenching was proportional to the amount of C2A added (Figure 4(B)). We also found fluorescence quenching by C2A was less pronounced in the presence of EDTA. As a control we also measured changes in fluorescence for samples mixed with the maltose binding protein (MBP) and found no significant change in fluorescence intensity (Figure S1(B)). This result suggests C2A-liposome interaction alters the distance between PI(4,5)P2 molecules, possibly due to changes in bilayer packing after domain insertion. We also observed fluorescence changes for liposomes lacking PS (PC:PI(4,5)P2:PI(4,5)P2-TopFluor 95:4.5:0.5) mixed with C2A (Figure S1(B)). To ensure that the observed fluorescence quenching was not due to TopFluor interaction with C2A, we repeated the measurements with PC:PC-TopFluor liposomes (99.5:0.5 ratio). We found that C2A did not induce a significant

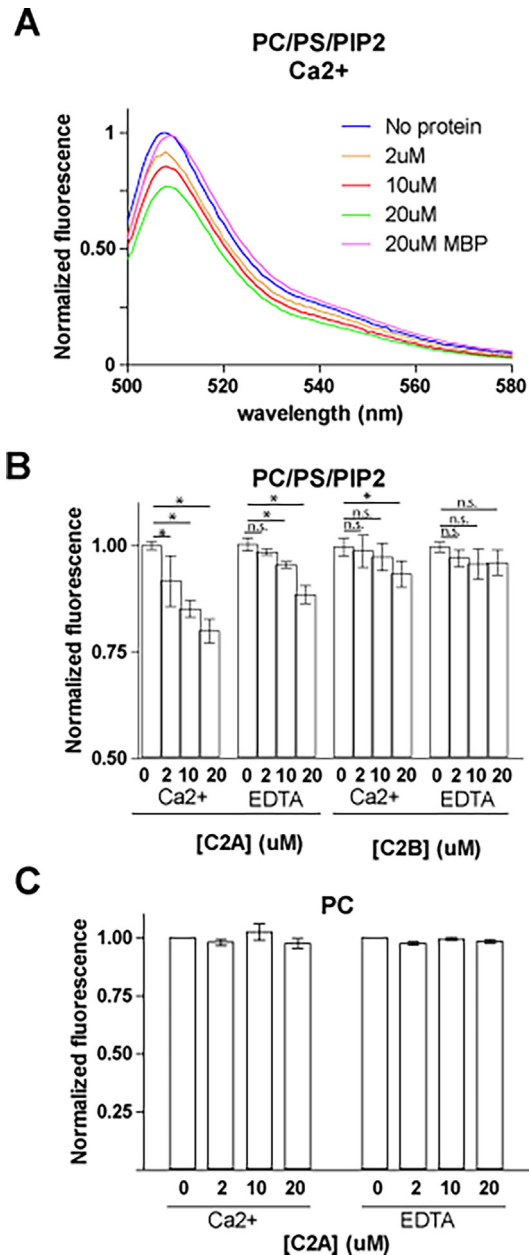


Figure 4. PI(4,5)P2-TopFluor quenches in the presence of C2A. (A) Representative titration of C2A mixed at the given concentration with liposomes composed of PC:PS:PI(4,5)P2:PI(4,5)P2-TopFluor (70:25:4.5:0.5). (B) Quantitation of PI(4,5)P2-TopFluor fluorescence intensity for C2A or C2B at the listed concentration in the presence of 250 μ M Ca²⁺ or 3 mM EDTA. (C) Quantitation of PC-TopFluor fluorescence intensity for C2A at the listed concentration in the presence of 250 μ M Ca²⁺ or 3 mM EDTA. ($N = 3$; error = \pm standard deviation; * $P < 0.05$).

change in fluorescence quenching of POPC-TopFluor at any of the C2A concentrations tested for either Ca²⁺ or EDTA conditions (Figure 4(C)). We conclude that subsequent to C2A binding to PI(4,5)P2 containing membranes, lipid rearrange-

ment occurs within the membrane resulting in a decrease in distance between labeled PI(4,5)P2 lipids.

Dysf C2A penetrates membranes

For some C2 domains, including those of synaptotagmin and DOC2, one or more Ca²⁺ binding loops insert and anchor the protein to the target membrane.^{33,34} To test whether dysf C2A inserts into membranes we measured the fluorescence from C2A variants that were labeled in the Ca²⁺ binding loop region (Figure 5(A)). C2A variants were generated by mutating positions 17 or 75 (C2A_{17acd}, C2A_{75acd}) within Ca²⁺ binding loops 1 or 3 to incorporate a TAG site to facilitate incorporation of the nonconical amino acid acridon-2-ylalanine (Acd), a fluorescent amino acid with an environmentally sensitive emission spectra.³⁵

When tested, we found that C2A_{75acd} fluorescence was blueshifted and the emission intensity increased (Figure 5(B,C)) when mixed with liposomes composed of PC:PS:PI(4,5)P2 (72.5:25:2.5 ratio). By contrast C2A_{17acd} displayed no blueshift and the increase in intensity was to a lesser extent when mixed with liposomes (Figure 5(D)). This increase in C2A_{75acd} fluorescence intensity is likely due to direct interaction with the membrane, however dequenching of Acd₇₅ by nearby aromatic residues like Tyr23 upon membrane-interaction could also contribute to the observed change. As an additional test for insertion, we measured C2A_{17acd} and C2A_{75acd} fluorescence when mixed with of PC:PS:PI(4,5)P2 liposomes containing either 1 mol% 5-doxy phosphocholine or 1% 12-doxy phosphocholine. The nitroxide spin label located at position 5 or 12 along the hydrophobic chain of this lipid quenches fluorophores that are located in close

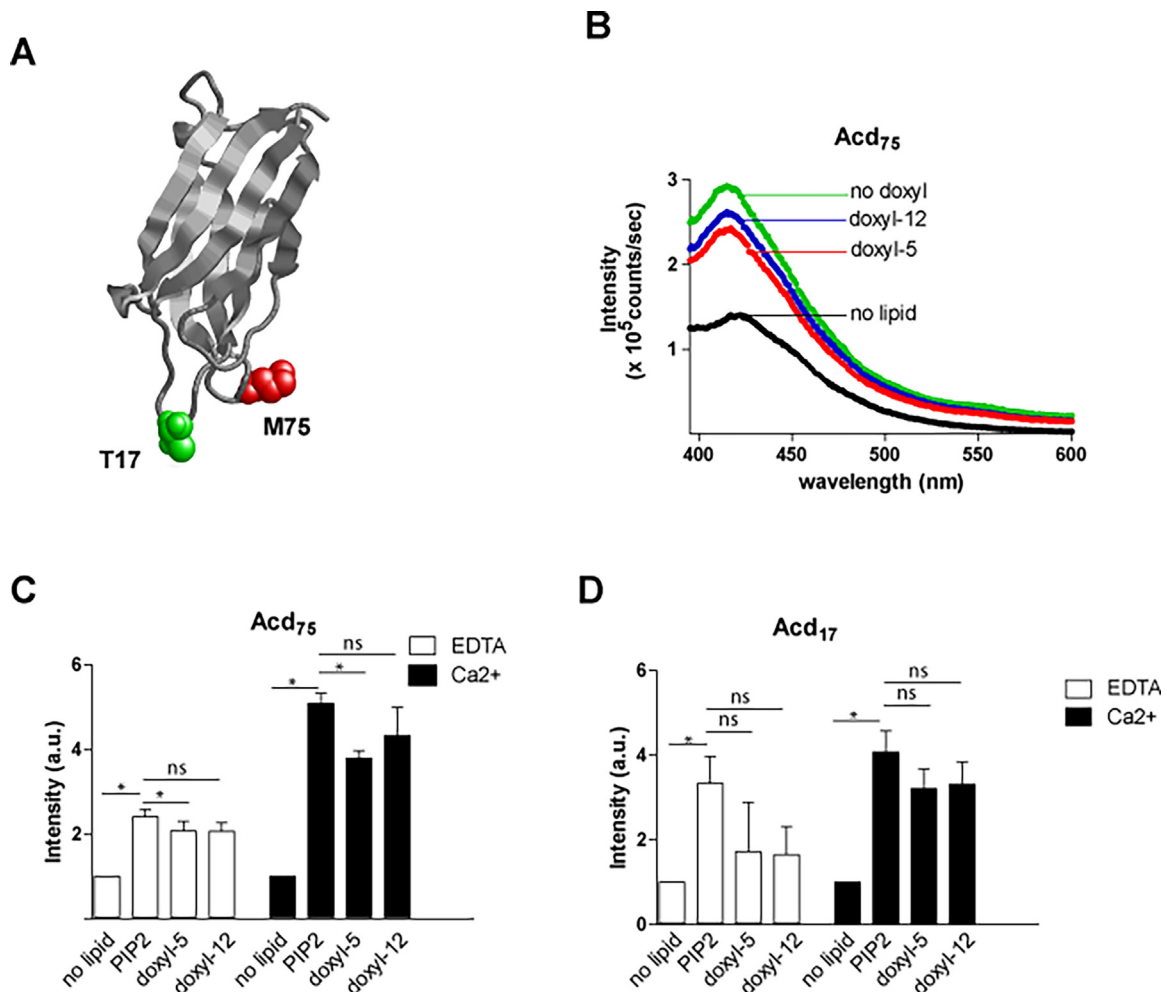


Figure 5. The Ca²⁺ binding loops of C2A insert into membranes. (A) Structure of dysf C2A (PDB 4IHB) highlighting residues T17 (green) and M75 (red) that were converted to TAG sites for Acd incorporation to generate Acd₁₇ and Acd₇₅. (B) Representative Acd₇₅ emission spectra when mixed with liposomes composed of PC:PS:PI(4,5)P2 (72.5: 25: 2.5 ratio), as well as PC:PS:PI(4,5)P2 liposomes with 1 mol% 5-doxy phosphocholine or 12-doxy phosphocholine. (C, D) Quantitation of (C) Acd₇₅ and (D) Acd₁₇ fluorescence in samples with conditions listed in (C) in the presence of 5 mM EDTA (white) or 1 mM Ca²⁺ (black). (*N* = 3; error = ±standard deviation; **P* < 0.01).

proximity.³³ As shown in Figure 5(C), addition of the 5-doxy lipid resulted in a significant reduction in fluorescence intensity for C2A_{75acd}, supporting the conclusion that C2A inserts into liposome membranes. The fluorescence intensity of C2A_{17acd} was also quenched in samples containing doxyl lipids but did not reach statistical significance (Figure 5(D)).

Resonance Assignments and IP3 titration. To identify residues that mediate C2A – PI(4,5)P2 interaction we applied solution NMR. We first analyzed [1H-15N]-TROSY spectra of isotopically labeled C2A (amino acids 1–129), and found the spectra well dispersed, indicating that the domain is folded (Figure S2(A,B)). We assigned 108 of the 120 non-proline residues, and of the unassigned residues, 75% (9 out of 12) were in the loop regions between β -strands. Of the remaining three residues two were located next to the C-terminus and one is adjacent to Ca²⁺ binding loop 3. We also measured the domain using Size Exclusion Chromatography-Multi Angle Light Scattering (SEC-MALS) and determined that the domain is monomeric under the conditions used for our NMR studies (Figure S2(C)). To gain insight into the influence of Ca²⁺ on the structure of C2A, we collected [1H-15N]-TROSY spectra of 15 N labeled dysferlin C2A samples at Ca²⁺ concentrations ranging from 0 to 5 mM Ca²⁺ (Figure S2(D)). Instead of fast exchange (μ sec) as has been reported for many C2 domains, lowering the Ca²⁺ concentration pushed residues in the Ca²⁺ binding loops into the immediate exchange regime³⁶⁻³⁸. We also found that lowering the Ca²⁺ concentration resulted in a significant decrease in peak intensity for all three CBL. Model free analysis of heteronuclear NOE revealed dynamics within the CBL regions, with S2 values below 0.8 in loop regions and the termini and higher values of 0.8 to 1.0 in regions of secondary structure (Figure S3 (A)). Chemical exchange (R_{ex}) values in the presence of 5 mM Ca²⁺ also suggest the protein retains flexibility within the loops implicated in binding Ca²⁺, a result consistent with the same regions having the highest B-factors in the reported crystal structures (Figure S3(B)).

We next tested the interaction between C2A and inositol triphosphate (IP3), a soluble form of the PI (4,5)P2 headgroup (Figure 6). IP3 was titrated into a sample containing 15 N labeled dysferlin C2A with Ca²⁺ or EDTA. The titration of the C2A domain with IP3 identified residues K32, K33, R34, and R77 that displayed significant chemical shift perturbations (CSP), ranging from 0.439 to the 1σ cut-off of 0.052 ppm, indicative of interaction between IP3 and C2A (Figure 6(A-C)) and correspond to the concave side of the domain. Fits to a single site binding model revealed Kd values ranging from 12 to 15 μ M in the presence of Ca²⁺ for CSP detected for K32, K33, and R77 (Figure 6(D)). We assumed a single

site binding model based on previous studies of similar C2 domains that also bind to a single lipid headgroup, and the relatively linear movement of the NMR resonances during our titration that suggests two-state fast exchange. We also found that the presence of EDTA reduced the interaction between C2A and IP3 upward of 10 fold for the same K32 and K33 residues. However, the CSP values for Ca²⁺ binding loop 3 which showed the largest shift upon addition of IP3 to the Ca²⁺ bound C2A, showed little or no shift in response to IP3 in the absence of Ca²⁺. These results suggest that Ca²⁺ modulates the affinity of C2A for the PI(4,5)P2 headgroup.

Calcium shifts the dynamic equilibrium of C2A between two distinct structural States.

Given the effects of Ca²⁺ on the C2A-IP3 interaction, we next sought to characterize the role of Ca²⁺ on the structure of C2A by collecting chemical exchange saturation transfer (CEST) measurements.⁽³⁹⁾ 15 N CEST experiments were performed at 1, 3, and 5 mM Ca²⁺ (Figure 7, Figures S4, S5, S6 and Tables S1, S2, S3). Chemical exchange was observed primarily in or near the Ca²⁺ binding loops at 5 mM Ca²⁺. Global modeling for these residues showed that 99.8% of the protein is in the Ca²⁺ bound state, with only 0.02% in the alternate state. At 3 mM Ca²⁺ we found 13 residues that showed CEST profiles with chemical exchange. Each of these profiles was individually fit to a two-state model of exchange and to a global two-state exchange model as described in the methods. The global modeling shows that at 3 mM Ca²⁺ dysferlin C2A is 97.6% in the Ca²⁺ bound state and 2.4% in the alternate state. At 1 mM Ca²⁺, many of the resonances exhibit reduced intensity, presumably due to chemical exchange. We followed 6 residues that showed chemical exchange by CEST and performed a similar modeling as used for the 3 mM Ca²⁺ data and determined the individual and global exchange parameters. Residues undergoing exchange were found to either be in the CBL regions or the concave face of the β -sandwich fold. As expected, the population distribution between states (87.5% vs. 12.5%) was shifted at low Ca²⁺ concentrations compared to high Ca²⁺. While we were unable to collect CEST measurements below 1 mM due to domain stability, our results clearly demonstrate that there is a Ca²⁺ sensitive dynamic equilibrium between two states for C2A.

Molecular dynamics simulations of C2A-membrane interaction

To gain further insight into the C2A-membrane complex, molecular dynamics (MD) simulations were conducted using the GROMACS simulation package.^{40,41} The C2A domain, including two

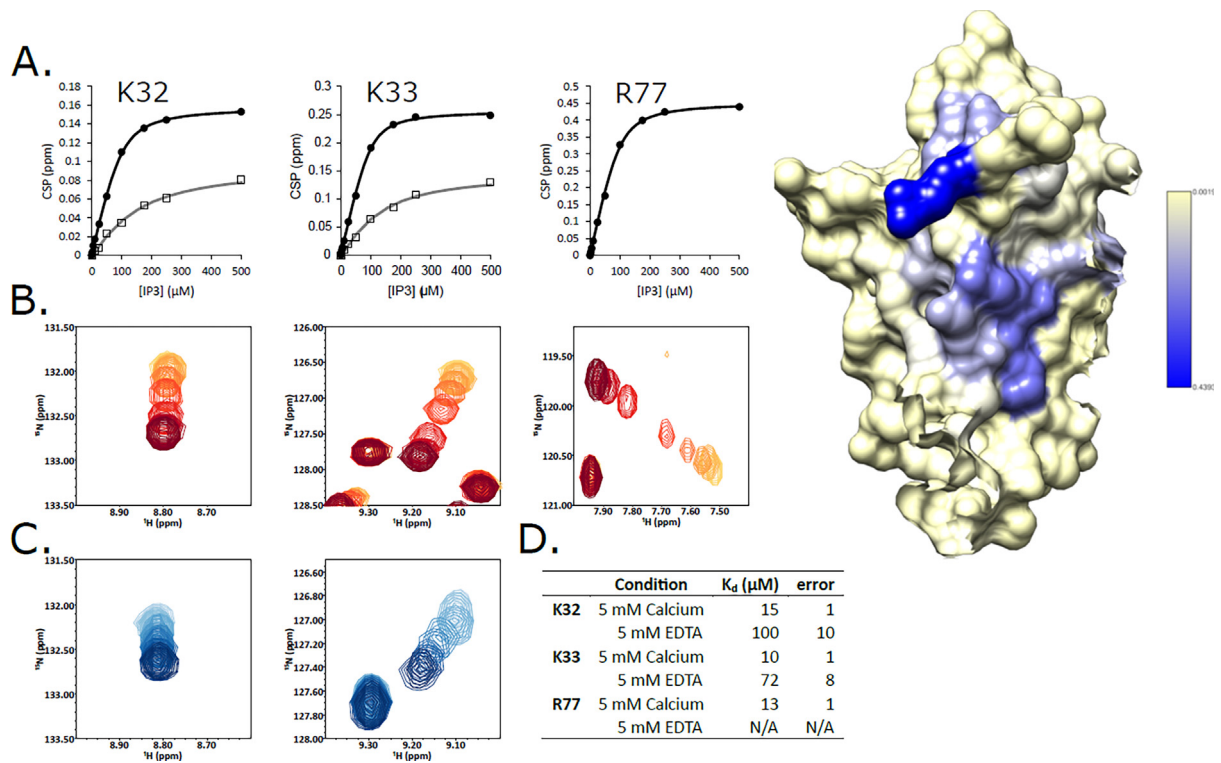


Figure 6. Titration of IP3 into Dysferlin C2A at high and low Ca^{2+} . (A) Representative titrations are shown for three residues, two in the basic patch and one in the Ca^{2+} binding loop. 5 mM Ca^{2+} data is shown in closed black circles, 5 mM EDTA data is shown in open squares. Fits to determine the K_d 's are shown in black and gray respectively. (B) Overlay of 15 N-TROSY spectra collected at increasing concentrations (light orange to dark orange) of IP3 in the presence of 5 mM CaCl_2 . (C) Overlay of 15 N-TROSY spectra collected at increasing concentrations (light blue to dark blue) of IP3 in the presence of 5 mM EDTA (low Ca^{2+}). (D) Table of IP3 binding affinities determined from the NMR titrations at high and low Ca^{2+} . Error is reported as \pm the value shown. The structure of dysferlin C2A (PDB 4IHB) with chemical shift perturbation ranging from the largest perturbation 0.439 (blue) to the 1σ cut-off of 0.052 ppm (yellow) is shown on the right.

bound Ca^{2+} ions, was simulated with symmetric membranes composed of PC:PS:PI(4,5)P2 (70:25:5 ratio) and 150 mM KCl. For each of the 5 simulations performed, the C2A domain was initially oriented perpendicular to the membrane surface with the Ca^{2+} binding loops positioned proximal to the bilayer. Over the span of the 500 ns of simulation time the C2A domain interacted with the bilayer and inserted into the membrane with the majority of changes occurring within the first 100 nsec of simulated time. A snapshot of C2A illustrating the position of the lysine residues and the Ca^{2+} binding loops relative to the membrane is shown in Figure 8 and Figure S7. We found that the number of hydrogen-bonds between C2A and the membrane increased over time as did the domain's tilt towards the membrane (Figure 8(C,D)). Further K32, K33, K34, and R77 were found to interact with PI(4,5)P2 lipids in all 5 simulations. The number of lipids that contacted the C2 domain also increased until plateauing at approximately 100 ns (Figure 8(E)). The increased number of lipid contacts is in agreement with the observed tilt angle that brings the concave side of the domain into contact with the

membrane (Figure 8(D)). Finally, we also quantitated the average insertion depth of the domain over the 500 ns time course of the simulations for positions T17 and M75 (Figure 8(F)). While T17 in loop 1 contacted the membrane, penetration of M75 in loop 3 was significantly deeper, with M75 inserting to a depth below the glycerol layer of the membrane. This result is in qualitative agreement with the Acd fluorescence measurements.

Discussion

In this study we find that Ca^{2+} both reduces the flexibility of C2A and promotes interaction with PI(4,5)P2 membranes. The interaction between C2A and PI(4,5)P2 would likely steer dysf to PI(4,5)P2 enriched membranes including t-tubules and the plasma membrane.⁽⁴²⁾ The loss of this steering activity may account for the reported functional deficiencies of truncated dysf lacking the C2A domain.^{18,42} The targeting of C2A to PI(4,5)P2 membranes could be aided by the long flexible linker at the C-terminus of the domain which may

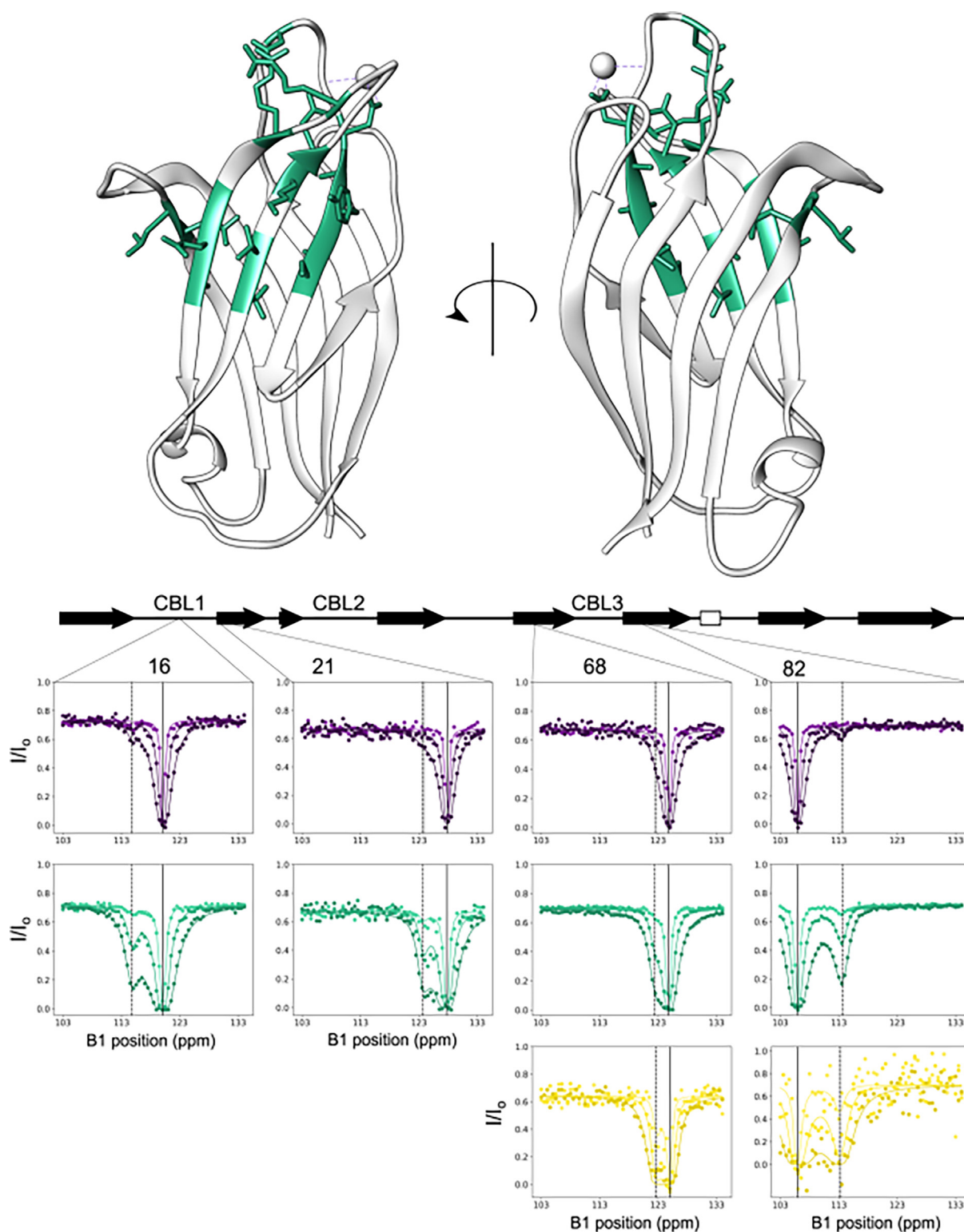


Figure 7. (A) residues exchanging at 3 mM CaCl₂ mapped onto the structure (4IHB). (B) Selected CEST traces showing increased exchange at lower Ca²⁺ concentrations. Data (circles) and fits (lines) for 50 (dark), 25 (medium), and 10 (light) Hz saturation field strengths. Solid vertical lines indicate the ¹⁵N chemical shift for the major state, dotted vertical lines indicate the ¹⁵N chemical shift for the minor state, with error indicated by grey shading.

allow C2A to search a large volume and increase the association rate for membranes. A similar

mechanism has been proposed for the linker region of the protein epsin during vesicle recycling.⁴³

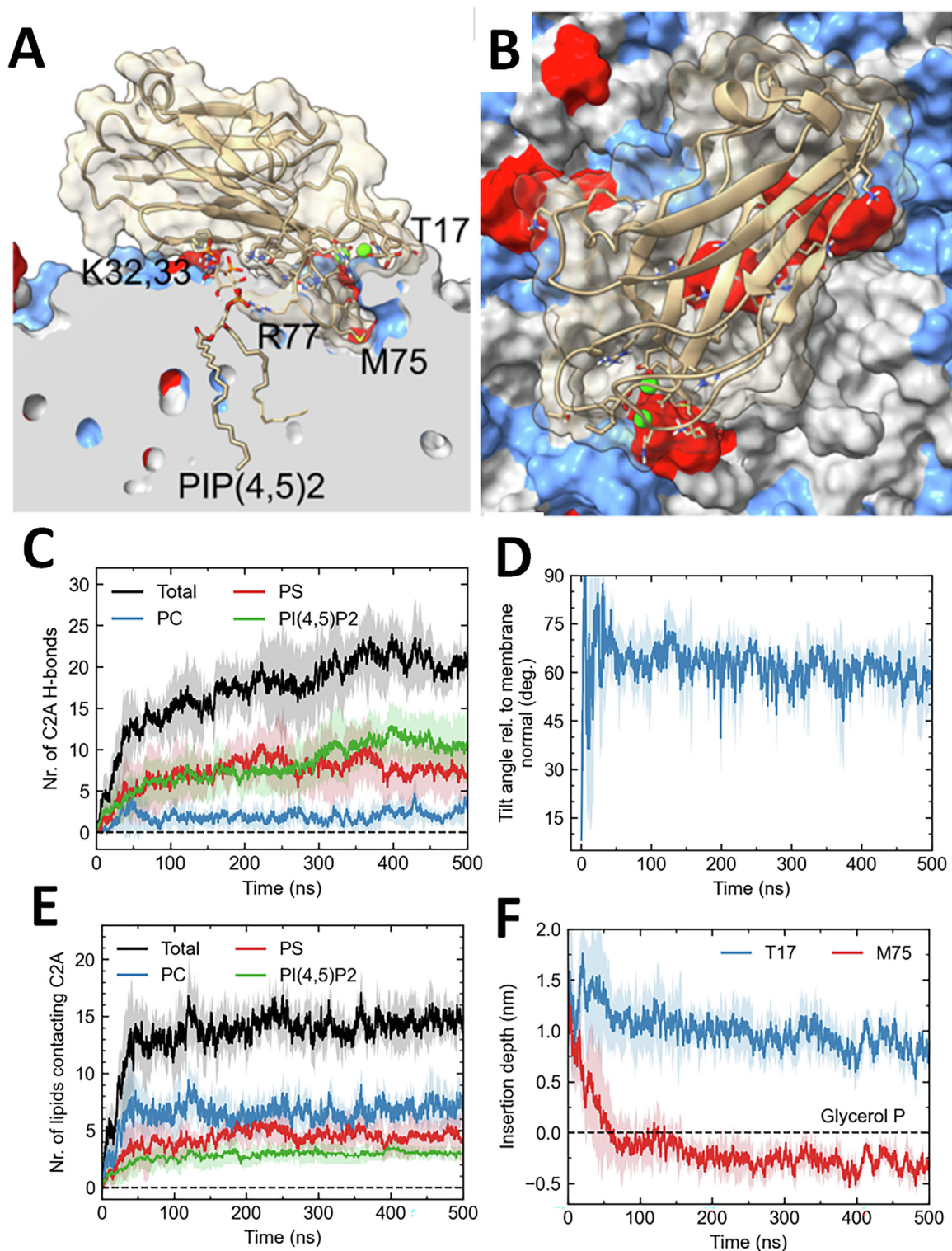


Figure 8. MD simulations of C2A domain (pdb 7JOF) with PC:PS:PI(4,5)P2 (70:25:5) membranes. (A) Representative cross section of membrane showing the interaction of C2A domain with a PI(4,5)P2 lipid. (B) Representative top-down orientation of C2A domain interacting with the membrane. PS lipids colored in blue and PIP (4,5)2 lipids colored in red. (C) Number of H-bonds between C2A domain and neighboring lipids. (D) Tilt angle of C2A domain relative to the membrane normal (see Methods). (E) Number of lipid molecules that contact the C2A domain. (F) Insertion depth for residues T17 and M75 relative to the depth of the glycerol phosphorous atom in the lipid membrane.

When bound to PI(4,5)P2, C2A may act as an anchor to bring the remaining C2 domains into close proximity with the membrane.

Based on our NMR results and MD simulations we propose that the PI(4,5)P2 binding interface includes residues Y23, K32, K33, R34, and R77 on the concave face of the β -sandwich fold, a region structurally similar to that found in PKC.⁴⁴ The main contact sites between dysf C2A and IP3 are ionic interactions between the identified amino acid sidechains and IP3, and the linear movement of the NMR resonances during the titration (Figure 6) is consistent with a 2-state model of fast exchange. Analysis of our titration data suggests Ca²⁺ boosts the binding affinity at K32 and K33 by approximately 7–10-fold. R77, which resides in the Ca²⁺ binding loop 3 region, did not display measurable interaction with IP3 in EDTA, however titrations in Ca²⁺ revealed a K_d value of 13 μ M. Analysis of our MD simulation data also suggests a role for the side chains of K32, K33, R34, and R77 in PI(4,5)P2 interaction (Figure 8, S7).

Based on sequence alignment several of the residues of C2A that appear to mediate interaction with PI(4,5)P2 are conserved in other PI(4,5)P2 binding C2 domains, including rabphilin 3a and PKC α .^{44,45} For PKC α , a stretch of basic residues within the C2 domain which align in sequence with K32 through K36 of dysf C2A mediate interaction with PI(4,5)P2. In addition dysf C2A R77 and N78 are conserved in PKC, and like dysf, contribute to PI(4,5)P2 interaction. These similarities suggest a shared structural basis for PI(4,5)P2 binding. Among the vertebrate ferlins, the basic K32 and K33 residues found in dysf C2A are found in myoferlin and Fer1L5, however both proteins show substitutions for Y23 and R77 found in dysf C2A (Figure S8). The lack of conservation may account for the reported inability of myoferlin C2A to bind PI(4,5)P2.²⁰ Less similar still is otoferlin C2A, which does not bind Ca²⁺ and does not display sequence similarity to dysf C2A.²¹ However tests on otoferlin have identified C2C and C2F as PI(4,5)P2 binding domains. PI(4,5)P2 binding activity may not be conserved across C2 domains of ferlin homologues.²⁴

Analysis of our CEST measurements reveal that several key residues within the C2A Ca²⁺ binding loop 3, as well as the concave face of the domain undergo increasing chemical exchange at lower Ca²⁺ concentration, suggesting that these residues are sampling a structurally different state. We speculate that Ca²⁺ enhances PI(4,5)P2 binding by switching C2A from a more dynamic, PI(4,5)P2 low affinity state, to a more rigid, PI(4,5)P2 high affinity state, where the β -strands in the concave face of the β -sandwich are stabilized for PI(4,5)P2 binding. The inositol phosphate sensitive residues identified in our study are distinct from the region of C2 domains that are thought to interact with PS, allowing for

simultaneous membrane interactions in the presence of Ca²⁺.

Multiple mutations identified within the dysf C2A domain have been linked to limb-girdle muscular dystrophy and Miyoshi myopathy. Among the known mutations, the most-well characterized is V67D, which varies in phenotypic severity among patients.⁴⁶ Exchange of the D residue at this position with a hydrophobic V results in loss of dysf membrane tubulation activity and T-tubule formation in muscle.⁸ Dysf mediated T-tubule biogenesis also requires PI(4,5)P2.⁸ Based on our Acd measurements as well as the results of MD simulations we conclude that the Ca²⁺ binding loop 3 of C2A penetrates membranes. For other C2 domain proteins like synaptotagmin and DOC2, membrane insertion by the PI(4,5)P2 binding C2 domain is required for protein activity.⁴⁷⁻⁴⁹ We therefore speculate that the V67D mutation results in a loss of C2A membrane binding and insertion, leading to the observed loss of tubulation activity.

Materials and Methods

Molecular Biology and Protein Purification.

Human dysferlin cDNA (GenBank accession no. **AF075575**), a gift from Dr. Kate Bushby (Newcastle University), was used as a template for cloning. The C2A domain (amino acids 1–129) was cloned into the pET28a (+) vector (Novagen) between the BamHI and HindIII restriction sites. Complementary flanking restriction sites for the dysferlin insert were generated by PCR amplification using the following primers: forward 5'-GCG CGC GGA TCC ATG CTG AGG GTC TTC ATC CTC TAT GCC-3' reverse 5'-GCG CGC AAG CTT TTA AGC TCC AGG CAG CGG-3'. BL21 DE3 cells harboring the expression plasmid were cultured overnight at 37 °C in Luria-Bertani broth containing 50 μ g/mL kanamycin and 1% w/v glucose and were used to seed 1 liter cultures of Luria-Bertani broth containing 50 μ g/mL kanamycin at a ratio of 1:1000. 15 N and 15 N/13C isotopically labeled protein was produced by bacteria grown in MJ9 media containing 1 g/L 15NH₄Cl and 2 g/L of 12C or 13C glucose. Cultures were then grown to an optical density of 0.6 at 37 °C and induced with 0.5 mM isopropyl β -D1-thiogalactopyranoside (IPTG). Protein was expressed for 16 hours at 18 °C. Cultures were centrifuged at 4000 rpm at 4 °C for 20 minutes and resuspended in lysis buffer: 50 mM HEPES pH 8, 250 mM NaCl, 10% (v/v) glycerol, 5 mM CaCl₂, 1 mM phenylmethanesulfonyl fluoride (PMSF), and 1 μ M leupeptin, pepstatin A, and aprotinin. Cells were lysed using a Microfluidics M–11P microfluidizer at 18,000 psi. 0.5% CHAPS (w/v) was added to the total lysate and left to rock for 1 hour on ice. Soluble fractions were then obtained by centrifugation in a Beckman J2-21 centrifuge at

20,000 × g at 4 °C for 20 minutes. Clarified lysate was bound to HisPur Cobalt resin (Thermo Scientific) for 2 hours with rocking at 4 °C. Beads were then washed with 20 column volumes of lysis buffer and protein was eluted with 50 mM HEPES, 150 mM NaCl, 5 mM CaCl₂, and 200 mM imidazole. Purity of the elution fractions was confirmed via SDS-PAGE, pooled, and dialyzed against 50 mM HEPES, 150 mM NaCl, 5 mM CaCl₂ and 1 mM 1,4-dithiothreitol (DTT). The hexahistidine purification tag was cleaved from isotopically labeled samples by thrombin during dialysis into a low salt buffer (50 mM HEPES, 20 mM NaCl, 5 mM CaCl₂, 1 mM DTT, pH 7). The cleaved protein was further purified by cation exchange chromatography (HiTrap™ SP HP, GE). Samples were then dialyzed into NMR buffer (50 mM HEPES, 100 mM KCl, 5 mM CaCl₂, 5 mM DTT, pH 7), concentrated, and supplemented with 1 mM sodium azide, 10% D₂O, and 2–2 dimethylsilapentane-5-sulfonic acid prior to data collection.

For the incorporation of the noncanonical amino acid acridon-2-ylalanine, mutagenesis was conducted on the pET28a(+) vector containing the human dysferlin C2A domain (amino acids 1 – 129). Codeons for Threonine 17 or methionine 75 were converted to a TAG site. Gibson assembly (New England Biolabs) was used to introduce single site mutation. The dysferlin C2A T17 and M75 constructs were co-transformed with the machinery plasmid pDule2 Acd Mj A9 into BL21-DE2 Escherichia coli cells. The bacterial cultures (OD₆₀₀ = 0.6) were induced for 15–18 h at 18 °C with 0.5 mM IPTG and 200 μM acridon-2-ylalanine. The cells were lysed by sonication in lysis buffer with DNase (10 μg/mL) and protease inhibitors (1 mM PMSF, 1–2 μg/mL aprotinin, leupeptin, and pepstatin A). The lysis buffer contained 25 mM HEPES, 150 mM NaCl, 5 mM CaCl₂, and 5 mM imidazole (pH 8.0). Total lysate was incubated with 0.5% 3-((3-cholamidopropyl)dimethylammonio)-1-propanesulfonate (CHAPS) (w/v) on an orbital shaker for 1 hour at 4 °C. The soluble fraction of the lysate was incubated with HisPur Cobalt resin (Thermo Scientific) for 1 h at 4 °C, and the Cobalt resin was washed with the following buffers at pH 8.0: (a) 25 mM HEPES, 150 mM NaCl, 5 mM CaCl₂, 10 mM imidazole, (b) 25 mM HEPES, 250 mM NaCl, 5 mM CaCl₂, 20 mM imidazole, and (c) 25 mM HEPES, 250 mM NaCl, 5 mM CaCl₂, 50 mM imidazole. The bound protein was eluted with buffer containing 25 mM HEPES, 100 mM NaCl, 5 mM CaCl₂, and 300 mM imidazole (pH 8.0). Purified proteins were buffer exchanged into 25 mM HEPES, 100 mM NaCl, and 1 mM CaCl₂ (pH 7.0) using Zeba Spin Desalting Column. Samples were analyzed by Sodium dodecyl sulfate–polyacrylamide gel electrophoresis (SDS–PAGE) gel for purity. Fluorescent acridon-2-ylalanine

incorporated proteins were imaged using BIO-RAD ChemiDoc MP Imaging System.

NMR Backbone Assignments. NMR spectra were collected at 303 K on a 800-MHz Bruker Avance IIIHD spectrometer equipped with a TC1 cryoprobe. Backbone resonance assignments were determined from a set of [15 N, 1H] TROSY based triple-resonance experiments. (HNCA, HNCACB, HNCOCACB, HNCO, HNCACO). NMR spectra were processed with NMRPipe and analyzed with CcpNmr Analysis.^{50,51} TALOS + was used to calculate secondary structure propensity.⁵² Chemical shifts have been deposited with the BMRB under accession number 50753. We note that NMR measurements were collected under conditions in which the measurement of T₂ values indicate the domain is a monomer.

NMR Titrations. Peak intensities for the titration experiments were normalized to the DSS signal to correct for changes in sample concentration. For the Ca²⁺ titration a sample in 5 mM CaCl₂ was back titrated with 0.5 mM EDTA (ethylenediaminetetraacetic acid) dissolved in NMR buffer lacking CaCl₂. D-myo-Inositol 1,4,5-tris–phosphate trisodium salt (Sigma-Aldrich) was dissolved in appropriate NMR buffer to stock concentrations of 2.057 or 20.57 mM and titrated to a final IP3:C2A ratio of 7.6:1. The chemical shift perturbation (CSP) was measured as the euclidean distance, with the nitrogen dimension weighted by a factor of 0.2.⁵³ For CSP mapping, CSP's were considered significant if the CSP was greater than 1 standard deviation (1σ). Residue 77 exhibited a large CSP, almost twice that of the next largest CSP, and was excluded from the calculation of the standard deviation to avoid over-biasing the calculation. For K_d measurements, the protein concentration was fixed at 98 μM and the IP3 concentration was varied up to 500 μM for the 5 mM CaCl₂ sample. For the K_d measurement at low calcium, the EDTA concentration was 5 mM and the maximum IP3 concentration was 2 mM. Chemical shift data were fit to a single site, fast-exchange binding model using nmrviewJ.

NMR Spin Relaxation. T₁ and T₂ 15 N relaxation times and steady-state 15 N-1H NOE values for all samples were obtained using standard [15 N, 1H] TROSY based Bruker pulse sequences with temperature compensation. Relaxation delay times for T₁ experiments varied from 20 ms to 1.2 s, relaxation delay times for T₂ experiments ranged from 33.9 ms to 271.4 ms. The steady-state 15 N–H NOE experiment included a total recovery delay of 8 seconds. Peak intensities were measured as peak heights, which were fit to a single exponential, $I = I_0 e^{-(rate \cdot t)}$, using CcpNMR Analysis to extract R₁ and R₂ values. NOE values were calculated by dividing peak intensity in the presence of amide saturation by peak intensity in the absence of amide saturation. Error (σ) in NOE values was calculated using the equation $\sigma_{NOE} = \frac{\sigma_{intensity}}{intensity}$.

NOE = $[(\delta_{\text{unsat}}/I_{\text{unsat}})^2 + (\delta_{\text{sat}}/I_{\text{sat}})^2]$ where δ is the baseline noise in each spectrum. Quadric diffusion was used to determine the diffusion tensor with PDB model 4IHB. We used FAST Modelfree to extract generalized order parameters and R_{ex} terms from spin-relaxation data.⁵⁴

Chemical Exchange Saturation Transfer (CEST) Measurements. 15 N CEST data was collected using a Bruker version of the published pulse sequence with saturation field strengths of 50, 25, and 10 Hz, with a saturation time of 0.4 seconds, and a 1.5 second recovery delay. A total of 64 planes were collected, 0.5 ppm steps from 103.0 ppm and 134.0 ppm and one reference plane. Fits to CEST intensity profiles were done using the ChemEx program (<https://github.com/gbouvnignies/chemex>).³⁹ Individual fits were made for each residue to a two-state exchange model, then residues where the error in exchange rate exceeded the exchange rate itself were rejected. The remaining residues yielded similar populations and exchange rates. We subsequently globally fit these residues to the two-state exchange model, yielding global exchange parameters. Gibbs free energies were calculated from the population differences. To identify additional residues that were in exchange, but where the chemical shift differences were small, we further fit the data for residues close to those previously fit in the global model, using the global exchange rate and populations as fixed parameters. This analysis resulted in the identification of 4 additional exchanging residues in the 3 mM Ca²⁺ sample.

Vibrational Sum-Frequency Spectroscopy. Sum-frequency spectra were recorded using a picosecond EKSPLA sum-frequency spectrometer, which utilizes a Nd:YAG laser operating at a 50 Hz repetition rate. The visible beam frequency was fixed at 532 nm while the infrared beam was tuned across the amide I and carbonyl vibrational regions (1570–1800 cm⁻¹). These beams, respectively, approached the lipid surface at incident angles of 60° and 54°. The sum-frequency response of interfacial proteins and lipids was spectrally filtered by a monochromator and detected with a photomultiplier tube. Each spectrum reported here was recorded in the SSP polarization combination and is the average of a minimum of 10 spectra, recorded over multiple days, with a step size of 2 cm⁻¹ and 300 acquisitions per step. In all experiments the lipid monolayer was established at the air–water interface. Lipids were deposited onto the surface of a D₂O buffer solution (50 mM HEPES, 150 mM NaCl, 1 mM DTT, 5 mM CaCl₂) and the interface was allowed to equilibrate for ~1 hour before dysferlin C2A was injected into the buffer subphase for a final C2A concentration of 5 μM. C2A was allowed to interact with the lipid surface for 3 hours before any VSF spectra were recorded of the protein-lipid surface.

Size Exclusion Chromatography-Multi Angle Light Scattering. Molecular mass was determined by size exclusion chromatography coupled multi angle light scattering on an AKTA Fast Protein Liquid Chromatography (FPLC) system (GE Healthcare Life Sciences) with a Superdex 200 10/300 GL column paired to a DAWN multi-angle light scattering instrument (Wyatt Technology) and Optilab differential refractometer (Wyatt Technology). All experiments were conducted at 25 and with a mobile phase consisting of 50 mM HEPES, 100 mM potassium chloride, 5 mM calcium chloride, and 1 mM DTT, pH 7.0. Protein samples were prepared at 30 μM concentration. Samples were injected onto the column at a flow rate of 0.8 mL/min and normalized differential refractive index and absolute molar mass was calculated using ASTRA software Ver. 8.0 (Wyatt Technology).

Fluorescence Measurements. Measurements were conducted using a QM-40 (Photon Technology International, Birmingham, NJ). We collected emission intensity from 400 to 600 nm for Acd measurements, 400–580 nm for TopFlor, and 400–500 nm for laurdan. Generalized polarization (GP) value was calculated using $GP = (I_{430} - I_{480}) / (I_{430} + I_{480})$. I₄₃₀ and I₄₈₀ are the emission intensities at 430 and 480 nm respectively. Data were collected using FelixGX set at 1.0 nm intervals with an integration time of 0.1 s.

Each sample was measured multiple times to ensure that the system was not changing over time. For Acd plots, Acd spectra were background subtracted and intensity integrated from 400 to 550 nm, and normalized to Acd fluorescence in the absence of liposomes.

MD simulations

Molecular dynamics (MD) simulations were carried out with the GROMACS simulation package v2021 using the CHARMM36 force-field (FF) for lipids and the CHARMM36m FF for proteins.^{40,55-57} Water was simulated with the modified CHARMM TIP3P parameters. The starting C2A domain structure (PDB ID: 7JOF) was obtained from Wang et al.²² All protein residues were simulated in their default protonation states at neutral pH. The C2A domain, including the two bound Ca²⁺ ions, was simulated with symmetric membranes composed of 1-palmitoyl-2-oleoyl-glycero-3-phosphocholine (POPC), 1-palmitoyl-2-oleoyl-glycero-3-phosphoserine (POPS), and 1-stearoyl-2-arachidonoyl-glycero-3-phospho(1'-myo-inositol-4',5'-bisphosphate) (PI(4,5)P₂). Each membrane leaflet was composed of 71 POPC lipids, 25 POPS lipids, and 6 PI(4,5)P₂ lipids to roughly match the experimental ratios. The combined protein-membrane system was setup using the CHARMM-GUI webserver.^{41,58} As the PI(4,5)P₂ lipid at neutral pH has one of the two sugar phos-

phates protonated (net headgroup charge of -4), we simulated it as two equal species were either of the phosphates at positions 4 or 5 are protonated (SAPI24 and SAPI25 in the CHARMM-GUI lipid library). Sufficient potassium and chloride ions were added to neutralize the system and have concentration corresponding to 150 mM KCl. For protein-membrane simulations, the C2A domain was oriented such that its principal axis was aligned with the membrane normal and the Ca²⁺ region was within a few angstroms from the membrane surface. Five different replicas with random initial positions of lipids were setup and simulated for 500 ns after initial energy minimization and equilibration using position restraints. Equations of motion were integrated with a leap-frog algorithm using a 2 fs time step. Van der Waals interactions were computed using a force-switched Lennard-Jones potential between 1.0 and 1.2 nm. Electrostatic interactions were computed using the particle-mesh Ewald method with a real space cutoff 1.2 nm and a Fourier grid spacing of 0.12 nm. Temperature was held constant with a time constant of 1 ps, and pressure was held constant with a stochastic cell-rescaling algorithm using a time constant of 5 ps. Particle positions were saved in 5 ps intervals for trajectory analysis.^{59,60}

Liposome preparation

Liposomes were prepared by first mixing chloroform dissolved lipids at the desired ratio in a glass tube and dried under vacuum to remove solvent. The dried lipids were subsequently rehydrated in a 20 mM Hepes-buffered solution containing 100 mM NaCl at pH ~ 7 and extruded using a polycarbonate membrane with a 50 nm cutoff. POPC, POPS, PI(4,5)P2 lipids, extruder, syringes, polycarbonate membranes and filter supports were purchased from Avanti Polar Lipids.

MD data analysis

To compute the C2A domain tilt angle we first defined a vector between the center of mass of protein residues near the Ca²⁺ binding loops (14–20 and 73–78) and the center of mass of protein residues on the other end (55–62 and 93–97). This vector then defined the tilt angle with respect to the membrane normal (the z axis). All figures were plotted using the Matplotlib library.⁶¹ Molecular models of the AT1 receptor were created using UCSF Chimera and ChimeraX.⁶²

Funding

This work was supported by the NIH National Institute of Deafness and Other Communication Disorders (NIDCD) Grant R01DC014588 and the National Science Foundation CHE 1905091, MCB 2019386, CHE 2137997, and CHE 137997. The Oregon State University NMR Facility is supported

in part by the National Institutes of Health, HEI Grant 1S10OD018518 and by M. J. Murdock Charitable Trust Grant 2014162. The content is solely the responsibility of the authors and does not necessarily represent the official views of the National Institutes of Health. This work was supported in part by the GCE4All Biomedical Technology Development and Dissemination Center supported by National Institute of General Medical Science grant RM1-GM144227.

CRedit authorship contribution statement

Ethiense Kwok: Methodology, Investigation, Validation, Formal analysis, Writing – original draft. **Sauna C. Otto:** Methodology, Investigation, Validation, Formal analysis, Writing – original draft. **Patricia Khuu:** . **Andrew P. Carpenter:** Methodology, Validation, Formal analysis, Resources, Writing – review & editing. **Sara J. Coddling:** . **Patrick N. Reardon:** Methodology, Validation, Formal analysis, Resources, Writing – review & editing. **Juan Vanegas:** Investigation, Formal analysis. **Tanushri M. Kumar:** Resources. **Chapman J. Kuykendall:** Resources. **Ryan A. Mehl:** Resources. **Joe Baio:** Conceptualization, Resources, Methodology, Writing – review & editing. **Colin P. Johnson:** Conceptualization, Formal analysis, Project administration, Funding acquisition.

DECLARATION OF COMPETING INTEREST

The authors declare that they have no known competing financial interests or personal relationships that could have appeared to influence the work reported in this paper.

Acknowledgements

We thank Elisar Barbar and James Petersson for constructive feedback.

Appendix A. Supplementary data

Supplementary data to this article can be found online at <https://doi.org/10.1016/j.jmb.2023.168193>.

Received 6 February 2023;
Accepted 27 June 2023;
Available online 3 July 2023

Keywords:
calcium;
dysferlin;
C2 domain;

CEST;
genetic code expansion

Authors contributed equally.

Abbreviations:

Dysf, dysferlin; MD, molecular dynamics; PS, 1-palmitoyl-2-oleoyl-*sn*-glycero-3-phosphoserine; PC, 1-palmitoyl-2-oleoyl-*sn*-glycero-3-phosphocholine; PI(4,5)P₂, phosphatidylinositol bisphosphate; PE, 1-palmitoyl-2-oleoyl-*sn*-glycero-3-phosphoethanolamin

References

- Bulankina, A.V., Thoms, S., (2020). Functions of Vertebrate Ferlins. *Cells* **9** <https://doi.org/10.3390/cells9030534>.
- Lek, A., Evesson, F.J., Sutton, R.B., North, K.N., Cooper, S.T., (2012). Ferlins: regulators of vesicle fusion for auditory neurotransmission, receptor trafficking and membrane repair. *Traffic* **13**, 185–194.
- Han, R., Rader, E.P., Levy, J.R., Bansal, D., Campbell, K. P., (2011). Dystrophin deficiency exacerbates skeletal muscle pathology in dysferlin-null mice. *Skelet. Muscle* **1**, 35.
- Kerr, J.P. et al, (2013). Dysferlin stabilizes stress-induced Ca²⁺ signaling in the transverse tubule membrane. *PNAS* **110**, 20831–20836.
- Bansal, D., Campbell, K.P., (2004). Dysferlin and the plasma membrane repair in muscular dystrophy. *Trends Cell Biol.* **14**, 206–213.
- Liu, J. et al, (1998). Dysferlin, a novel skeletal muscle gene, is mutated in Miyoshi myopathy and limb girdle muscular dystrophy. *Nature Genet.* **20**, 31–36.
- Bansal, D., Miyake, K., Vogel, S.S., Groh, S., Chen, C.-C., Williamson, R., McNeil, P.L., Campbell, K.P., (2003). Defective membrane repair in dysferlin-deficient muscular dystrophy. *Nature* **423**, 1–5.
- Hofhuis, J. et al, (2017). Dysferlin mediates membrane tubulation and links T-tubule biogenesis to muscular dystrophy. *J. Cell Sci.* **130**, 841–852.
- Han, W.Q. et al, (2012). Lysosome fusion to the cell membrane is mediated by the dysferlin C2A domain in coronary arterial endothelial cells. *J. Cell Sci.* **125**, 1225–1234.
- Dominguez, M.J., McCord, J.J., Sutton, R.B., (2022). Redefining the architecture of ferlin proteins. *Biophys. J.* **121**, 47a.
- Jumper, J. et al, (2021). Highly accurate protein structure prediction with AlphaFold. *Nature* **596**, 583–589.
- Chapman, E.R., Davis, A.F., (1998). Direct interaction of a Ca²⁺-binding loop of synaptotagmin with lipid bilayers. *J. Biol. Chem.* **273**, 13995–14001.
- Evans, J.H., Murray, D., Leslie, C.C., Falke, J.J., (2006). Specific translocation of protein kinase Ca to the plasma membrane requires both Ca²⁺ and PIP₂ recognition by its C2 domain. *Mol. Biol. Cell* **17**, 56–66.
- Nalefski, E.A. et al, (2001). C2 domains from different Ca²⁺ signaling pathways display functional and mechanistic diversity. *Biochemistry* **40**, 3089–3100.
- Fuson, K. et al, (2014). Alternate splicing of dysferlin C2A confers Ca²⁺-dependent and Ca²⁺-independent binding for membrane repair. *Structure* **22**, 104–115.
- Abdullah, N., Padmanarayana, M., Marty, N.J., Johnson, C.P., (2014). Quantitation of the calcium and membrane binding properties of the C2 domains of dysferlin. *Biophys. J.* **106**, 382–389.
- Therrien, C., Di, F.S., Pickles, S., Sinnreich, M., (2009). Characterization of lipid binding specificities of dysferlin C2 domains reveals novel interactions with phosphoinositides. *Biochemistry* **48**, 2377–2384.
- Muriel, J. et al, (2022). The C2 domains of dysferlin: roles in membrane localization, Ca²⁺ signalling and sarcolemmal repair. *J. Physiol.* **600**, 1953–1968.
- De Luna, N. et al, (2007). Dysferlin expression in monocytes: A source of mRNA for mutation analysis. *Neuromuscul. Disord.* **17**, 69–76.
- Harsini, F.M. et al, (2019). Structural Basis for the Distinct Membrane Binding Activity of the Homologous C2A Domains of Myoferlin and Dysferlin. *J. Mol. Biol.* **431**, 2112–2126.
- Helfmann, S. et al, (2011). The crystal structure of the C2A domain of otoferlin reveals an unconventional top loop region. *J. Mol. Biol.* **406**, 479–490.
- Wang, Y. et al, (2021). Calcium binds and rigidifies the dysferlin C2A domain in a tightly coupled manner. *Biochem. J.* **478**, 197–215.
- Mandal, K., (2020). Review of PIP₂ in cellular signaling, functions and diseases. *Int. J. Mol. Sci.* **21**, 1–20.
- Padmanarayana, M. et al, (2014). Characterization of the lipid binding properties of otoferlin reveals specific interactions between PI(4,5)P₂ and the C2C and C2F Domains. *Biochemistry* **53**, 5023–5033.
- Marty, N.J., Holman, C.L., Abdullah, N., Johnson, C.P., (2013). The C2 domains of otoferlin, dysferlin, and myoferlin alter the packing of lipid bilayers. *Biochemistry* **52**, 5585–5592.
- Nguyen, K.T., King, J.T., Chen, Z., (2010). Orientation determination of interfacial β -sheet structures in situ. *J. Phys. Chem. B* **114**, 8291–8300.
- Lambert, A.G., Davies, P.B., Neivandt, D.J., (2005). Implementing the theory of sum frequency generation vibrational spectroscopy: A tutorial review. *Appl. Spectrosc. Rev.* **40**, 103–145.
- Buffeteau, T. et al, (2000). Anisotropic Optical Constants of α -Helix and β -Sheet Secondary Structures in the Infrared. *J. Phys. Chem. B* **104**, 4537–4544.
- Fu, L. et al, (2015). Characterization of parallel β -sheets at interfaces by chiral sum frequency generation spectroscopy. *J. Phys. Chem. Letter* **6**, 1310–1315.
- Golbek, T.W. et al, (2019). Otoferlin C2F Domain-Induced Changes in Membrane Structure Observed by Sum Frequency Generation. *Biophys. J.* **117**, 1820–1830.
- Golbek, T.W. et al, (2021). Direct Evidence That Mutations within Dysferlin's C2A Domain Inhibit Lipid Clustering. *J. Phys. Chem. B* **125**, 148–157.
- Egea-Jiménez, A.L. et al, (2014). Phosphatidylinositol-4,5-bisphosphate enhances anionic lipid demixing by the C2 domain of PKC α . *PLoS One* **9** <https://doi.org/10.1371/journal.pone.0095973>.
- Bradberry, M.M., Bao, H., Lou, X., Chapman, E.R., (2019). Phosphatidylinositol 4,5-bisphosphate drives Ca²⁺-independent membrane penetration by the tandem C2 domain proteins synaptotagmin-1 and Doc2. *J. Biol. Chem.* **294**, 10942–10953.

34. Hui, E., Bai, J., Chapman, E.R., (2006). Ca²⁺-triggered simultaneous membrane penetration of the tandem C2-domains of synaptotagmin I. *Biophys. J.* **91**, 1767–1777.
35. Jones, C.M., Petersson, G.A., Petersson, E.J., (2021). Synthesis and characterization of fluorescent amino acid dimethylaminoacridonylalanine. *ARKIVOC* **2021**, 97–109.
36. Shao, X., Davletov, B.A., Sutton, R.B., Südhof, T.C., Rizo, J., (1996). Bipartite Ca²⁺-binding motif in C2 domains of synaptotagmin and protein kinase C. *Science (80-)* **273**, 248–251.
37. Garcia, J., Gerber, S.H., Sugita, S., Südhof, T.C., Rizo, J., (2004). A conformational switch in the Piccolo C2A domain regulated by alternative splicing. *Nature Struct. Mol. Biol.* **11**, 45–53.
38. Yagi, H. et al, (2015). Structural basis for Ca²⁺-mediated interaction of the Perforin C2 domain with lipid membranes. *J. Biol. Chem.* **290**, 25213–25226.
39. Vallurupalli, P., Bouvignies, G., Kay, L.E., (2012). Studying “invisible” excited protein states in slow exchange with a major state conformation. *J. Am. Chem. Soc.* **134**, 8148–8161.
40. Abraham, M.J. et al, (2015). Gromacs: High performance molecular simulations through multi-level parallelism from laptops to supercomputers. *SoftwareX* **1–2**, 19–25.
41. Lee, J. et al, (2016). CHARMM-GUI Input Generator for NAMD, GROMACS, AMBER, OpenMM, and CHARMM/OpenMM Simulations Using the CHARMM36 Additive Force Field. *J. Chem. Theory Comput.* **12**, 405–413.
42. Lukyanenko, V.I., Muriel, J.M., Bloch, R.J., (2020). Effect of Bapta and Dysferlin’s C2A Domain on Recovery of Ca²⁺D Transients After Osmotic Shock in Dysferlin-Null Myofibers. *Biophys. J.* **118**, 35a.
43. Pietrosevoli, N., Pancsa, R., Tompa, P., (2013). Structural Disorder Provides Increased Adaptability for Vesicle Trafficking Pathways. *PLoS Comput. Biol.* **9** <https://doi.org/10.1371/journal.pcbi.1003144>.
44. Guerrero-Valero, M. et al, (2009). Structural and mechanistic insights into the association of PKC α -C2 domain to PtdIns(4,5)P₂. *PNAS* **106**, 6603–6607.
45. Guillén, J. et al, (2013). Structural insights into the Ca²⁺ and PI(4,5)P₂ binding modes of the C2 domains of rabphilin 3A and synaptotagmin 1. *PNAS* **110**, 20503–20508.
46. Illarioshkin, S.N. et al, (2000). Identical dysferlin mutation in limb-girdle muscular dystrophy type 2B and distal myopathy. *Neurology* **55**, 1931–1933.
47. Koldsø, H., Shorthouse, D., Hélie, J., Sansom, M.S.P., (2014). Lipid Clustering Correlates with Membrane Curvature as Revealed by Molecular Simulations of Complex Lipid Bilayers. *PLoS Comput. Biol.* **10** <https://doi.org/10.1371/journal.pcbi.1003911>.
48. Paddock, B.E. et al, (2011). Membrane penetration by synaptotagmin is required for coupling calcium binding to vesicle fusion in vivo. *J. Neurosci.* **31**, 2248–2257.
49. Hui, E., Johnson, C.P., Yao, J., Dunning, F.M., Chapman, E.R., (2009). Synaptotagmin-Mediated Bending of the Target Membrane Is a Critical Step in Ca²⁺-Regulated Fusion. *Cell* **138**, 709–721.
50. Delaglio, F. et al, (1995). NMRPipe: A multidimensional spectral processing system based on UNIX pipes. *J. Biomol. NMR* **6**, 277–293.
51. Vranken, W.F. et al, (2005). The CCPN data model for NMR spectroscopy: Development of a software pipeline. *Proteins Struct. Funct. Genet.* **59**, 687–696.
52. Shen, Y., Delaglio, F., Cornilescu, G., Bax, A., (2009). TALOS+: A hybrid method for predicting protein backbone torsion angles from NMR chemical shifts. *J. Biomol. NMR* **44**, 213–223.
53. Williamson, M.P., (2013). Using chemical shift perturbation to characterise ligand binding. *Prog. Nucl. Magn. Reson. Spectrosc.* **73**, 1–16.
54. Cole, R., Loria, J.P., (2003). FAST-Modelfree: A program for rapid automated analysis of solution NMR spin-relaxation data. *J. Biomol. NMR* **26**, 203–213.
55. Klauda, J.B. et al, (2010). Update of the CHARMM All-Atom Additive Force Field for Lipids: Validation on Six Lipid Types. *J. Phys. Chem. B* **114**, 7830–7843.
56. Huang, J. et al, (2016). CHARMM36m: An improved force field for folded and intrinsically disordered proteins. *Nature Methods* **14**, 71–73.
57. MacKerell, A.D. et al, (1998). All-atom empirical potential for molecular modeling and dynamics studies of proteins. *J. Phys. Chem. B* **102**, 3586–3616.
58. Wu, E.L. et al, (2014). CHARMM-GUI membrane builder toward realistic biological membrane simulations. *J. Comput. Chem.* **35**, 1997–2004.
59. Bussi, G., Donadio, D., Parrinello, M., (2007). Canonical sampling through velocity rescaling. *J. Chem. Phys.* **126** <https://doi.org/10.1063/1.2408420>.
60. Bernetti, M., Bussi, G., (2020). Pressure control using stochastic cell rescaling. *J. Chem. Phys.* **153** <https://doi.org/10.1063/5.0020514>.
61. Hunter, J.D., (2007). Matplotlib: A 2D graphics environment. *Comput. Sci. Eng.* **9**, 90–95.
62. Pettersen, E.F. et al, (2004). UCSF Chimera – A visualization system for exploratory research and analysis. *J. Comput. Chem.* **25**, 1605–1612.